

Iron *K*-edge anomalous small-angle X-ray scattering at 15-ID-D at the Advanced Photon Source

Nigel Kirby,^{a,b*} David Cookson,^{c,d} Craig Buckley,^b Eliza Bovell^e and Tim St Pierre^e

^aAustralian Synchrotron, 800 Blackburn Road, Clayton 3168, Australia, ^bDepartment of Imaging and Applied Physics, Curtin University of Technology, Bentley 6102, Australia, ^cAustralian Synchrotron Research Programme, Australia, ^dChemMatCARS, Advanced Photon Source, Argonne, IL 60439, USA, and ^eSchool of Physics, The University of Western Australia, Crawley 6009, Australia. Correspondence e-mail: nigel.kirby@synchrotron.vic.gov.au

Small-angle X-ray scattering (SAXS) is an ideal technique for characterizing inorganic nanoparticles in biological specimens large enough to be representative of tissues. As tissues consist of complex mixtures of structures, identifying particular structural features from single-wavelength scattering data can be problematic. Synchrotron SAXS can supply element-specific structural information in complex samples, using anomalous scattering close to absorption edges. Anomalous dispersion is a secondary effect that produces relatively subtle changes in scattering patterns. In order to utilize this effect for anomalous SAXS analysis, stringent control of instrument performance is required. This work outlines the development of high-quality data collection and processing strategies for Fe *K*-edge anomalous SAXS on the ChemMatCARS beamline at the Advanced Photon Source (APS), Chicago, with an emphasis on intensity normalization. The methods reported here were developed during a study of iron-loaded mammal tissues, but could equally well be applied to other complex specimens.

© 2007 International Union of Crystallography
Printed in Great Britain – all rights reserved

1. Introduction

Iron-overload diseases such as haemochromatosis and thalassaemia affect approximately 1 in 250 people (Halliday & Powell, 1992). These disorders result in excessive iron deposition in tissues in the form of ultrafine (5 to 10 nm) particles of iron(III) oxyhydroxide associated with the iron storage compounds haemosiderin and ferritin (Fig. 1). Excessive deposits of iron are toxic because they catalyse cell-damaging reactions such as lipid peroxidation (Grootveld *et al.*, 1989). Organs particularly affected by iron overload are the liver, heart, pancreas, spleen and adrenal gland. Knowledge of body iron loadings is of primary clinical importance in the management of haemochromatosis and thalassaemia.

This research is aimed at elucidating particle size and clustering effects of iron oxide particles in mammalian liver tissue, both to support application of magnetic resonance imaging techniques for non-invasive diagnosis and to obtain fundamental information about the nature of disease processes. Histological studies [*i.e.* using optical microscopy and transmission electron microscopy (TEM)], although useful for preliminary investigations, have limitations owing to the very small region of tissue sampled and to the somewhat subjective interpretation of images, particularly for particles clustered together. These difficulties may be overcome using small-angle X-ray scattering (SAXS) techniques, which analyse specimen volumes many orders of magnitude larger than TEM (typically $\gg 10^6$).

Previous measurements at a single energy, both on a laboratory SAXS camera and the ChemMatCARS camera (Fig. 2), showed a pronounced shoulder at a modulus q of the scattering vector [$q = 4\pi\sin(\phi/2)/\lambda$] of 0.06 \AA^{-1} and a peak at 0.13 \AA^{-1} . The intensity of the shoulder increased with increasing iron loading, unlike the peak

which showed no clear correlation with iron loading. The correlation between the size of the shoulder and iron loading could either be due to the presence of iron-rich particles, or an association arising from secondary biological effects on tissue structure caused by iron exposure. Anomalous small-angle X-ray scattering (ASAXS) allows this uncertainty to be resolved.

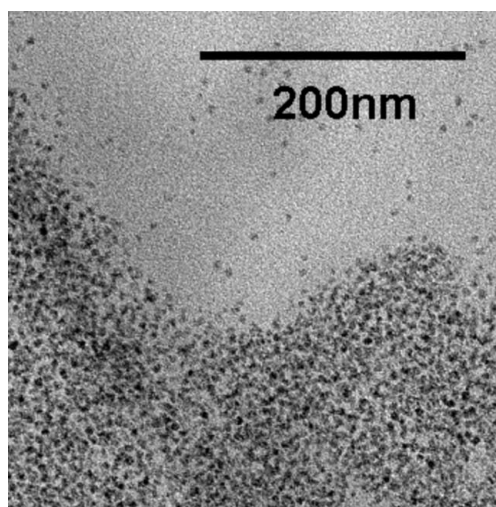


Figure 1
TEM image of iron-loaded liver tissue ($40.6 \text{ mg Fe g}^{-1}$), showing dispersed and densely packed iron-rich particles. Individual particles were 5.3 ± 0.8 (1σ) nm diameter.

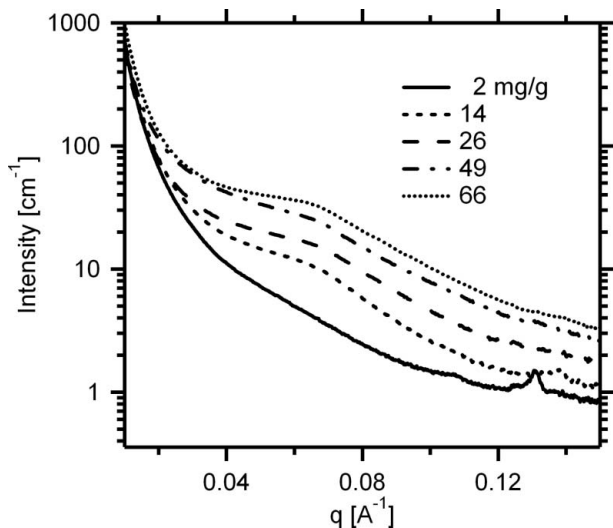


Figure 2
SAXS patterns of rat liver specimens measured at fixed energy (6.900 keV), displaying a monotonic increase in the size of the Guinier knee at $\sim 0.06 \text{ \AA}^{-1}$ with tissue iron concentration in mg Fe g^{-1} dry weight. 2 mg Fe g^{-1} is the non-iron-loaded control specimen.

With many sources of scattering contributing to the overall scattering pattern, single-wavelength SAXS data are difficult to interpret unambiguously. The iron oxide particles comprise only a small volume fraction of specimens, even at the highest levels of iron loading. Much of the total scattering intensity must therefore arise from complex soft-tissue structures, which must somehow be distinguished from the iron particles.

ASAXS may be used to vary the scattering contrast between the iron nanoparticles and their surrounding organic matrix. The scattering factor of a single atom is a function of the scattering vector q and photon energy E , and is given by:

$$f_{q,E} = f_q^0 + f'_E + f''_E$$

where f_q^0 is the atomic form factor (equal to the atomic number at $q = 0$), and f' and f'' are the real (elastic scattering power) and imaginary (absorption) parts of the dispersion corrections (Als-Nielsen & McMorrow, 2001). In the small-angle region, f can be approximated as angle independent. Element-specific contrast variation makes use

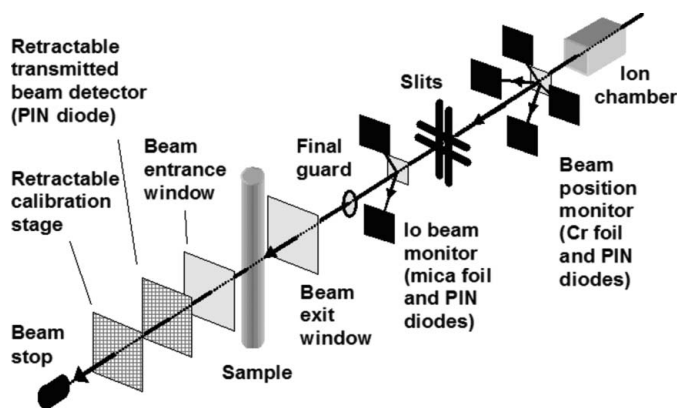


Figure 3
Detector layout of 15-ID-D. The CCD (omitted for clarity) is positioned approximately 10 cm downstream from the beamstop.

of the variation in f' with E , which is significantly greater for an element close to its absorption edge than any other elements that may be in the specimen.

ASAXS is an emerging technique which has been used mainly in the materials sciences, such as metallurgy (Jemian, 1990; Servant *et al.*, 1989), catalysis (Berg Rasmussen *et al.*, 2000, 2004) and glass science (Bruckner *et al.*, 1995; Krosigk *et al.*, 2001). While ASAXS has been used for the analysis of ferritin in solution (Stuhrmann, 1981), no such studies of ferritins in tissues have been reported to date. In-tissue analysis is necessary to study any particle clustering effects.

ASAXS experiments are simple in principle, but as any anomalous variations in scattering intensity are unlikely to exceed a few percent, real measurements place considerable demands on the reproducibility of scattering intensity calibration and normalization. To allow normalization between different exposures which may entail variations of incident-beam intensity and sample transmission, a number of different types of detectors and carefully executed data-collection strategies are required. The focus of this paper is the development of a reliable ASAXS measurement technique, from which the scientific outcomes for iron-overload disease will be reported elsewhere.

2. Instrument characterization

Beamline 15-ID-D at the APS comprises an 'undulator A' source, a flat diamond (111) double-crystal monochromator, two mirrors for vertical focusing and steering, and numerous beam-defining and antiscatter slits. The details of the overall beamline configuration are provided elsewhere (Cookson *et al.*, 2006). The location of the detectors is shown in Fig. 3. The area detector used for these measurements was a Bruker 6000 CCD with 1024×1024 pixels, effectively $92 \times 92 \mu\text{m}$ in size. The instrument is controlled using the software package *SAXS1D* (<http://cars9.uchicago.edu/chemmat/pages/swsoftware.html>), which is also used for primary data processing. An off-line version of this software is available to the public for the extraction, normalization and correction of image-based scattering data.

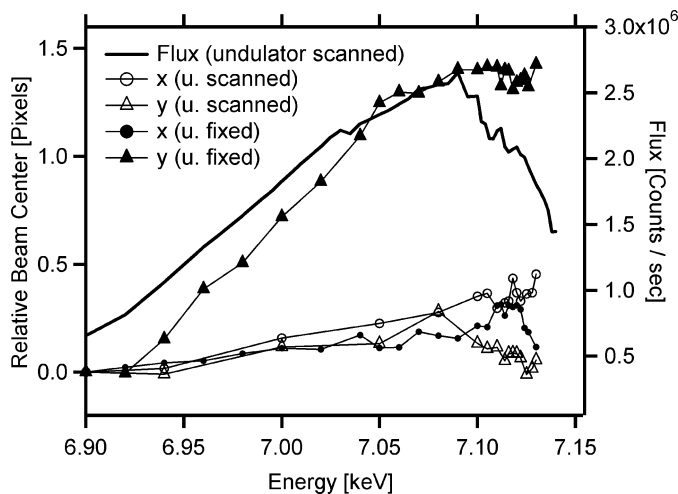


Figure 4
Effect of undulator operation on beam position as a function of energy at 1875 mm camera length. Data taken with beam-position feedback control in operation. 1 pixel = $92 \mu\text{m}$.

2.1. Beam centres

Accurate and precise measurement of beam centres is important for accurate radial integration of isotropic scattering data, especially if data close to the beam stop are required. When changing undulator and monochromator energy between exposures, small drifts in beam position can affect the calibration of the q scale. The software at ChemMatCARS has several algorithms for determining beam centres, the most useful one for this purpose utilizing MCM-41 isotropic scattering samples that can either be placed at the specimen position, or inside the camera flight tube using an automatically actuated stage. MCM-41 is a mesoporous silica with a highly ordered and narrow pore-size distribution producing diffraction rings with uniform radial intensity distribution (Sheppard *et al.*, 2005).

Systematic variations in beam centre with changing photon energy are shown in Fig. 4. The precision of fitting individual beam centres and the temporal stability of the beam position over a 20 min period were both ± 0.04 pixels ($4 \mu\text{m}$, 1σ). Since beam-centre fitting errors are comparable with temporal beam-position stability, it is sufficient to fit the beam centre only once per energy change.

Finding the beam centre for every new energy step was an effective way of tracking the behaviour of the undulator beam over an energy scan. Fig. 4 clearly shows the necessity of incrementing the undulator gap as well as the monochromator setting in order to achieve optimal beam stability when scanning beam energy. With a fixed undulator gap, the change in the vertical beam-centre position shows correlation with the beam intensity. Some of the shift in beam position (seen with both stationary and moving undulator gaps) can be attributed to increased heat loading on the first cooled crystal of the monochromator as its angle changes; this is sometimes not entirely eliminated by feedback from the beam-position monitor. Most of the additional drift seen for a stationary gap, however, is most likely due to the mode structure of the undulator A beam, which changes as one moves in energy over the harmonic.

2.2. Incident beam monitor

Incident flux (I_0) is measured using the forward scatter from a thin mica foil located prior to the exit window just before the specimen

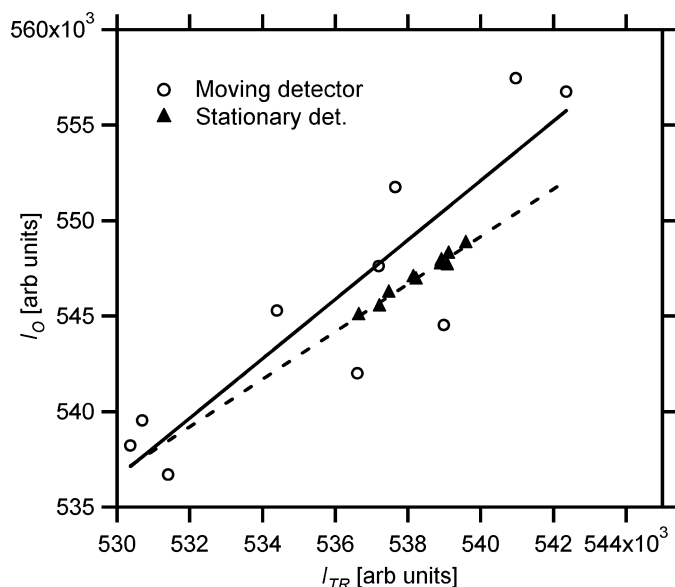


Figure 5 Correlation analysis of I_0 and I_{TR} , showing the inherent combined precision of I_0 and I_{TR} , and the reduced correlation due to I_{TR} repositioning errors.

space. Diffraction spots from the foil hit an array of four photodiodes, the output of which is summed and converted to transistor–transistor logic pulses which can be counted during an exposure. The fact that the mica foil is a single crystal means that, for routine operation, almost no detectable parasitic scatter is generated by this element in the camera.

Unfortunately, when scanning the beam energy, the diffraction spots hitting the photodiode array tend to move, providing a source of variability. The output from the mica foil-based I_0 detector drifts with increasing energy (10–40%, depending on beam size) compared with the output of a photodiode intercepting the main beam just after the specimen position. A sudden 100% increase in output from the I_0 detector arises from the presence of iron in the mica foil, which fluoresces when the beam energy reaches the K -edge at 7.12 keV.

Fortunately, this variability of output with energy is not seen from the array of photodiodes used further upstream to monitor beam position. In this case, the scattering foil is chromium, and the photodiodes give a difference-over-sum measurement which is used as dynamic feedback to a piezoelectric actuator on the second crystal in the monochromator. While this detective element is relatively insensitive to energy changes over a typical SAXS range, it does produce significant SAXS scatter, which must be removed by downstream slits. This would therefore make it highly unsuitable as a pre-sample detector for I_0 .

2.3. Specimen transmission measurement

Specimen transmission for fixed-wavelength experiments at ChemMatCARS is normally determined from simultaneous measurement of the ratio of I_0 to I_{TR} (incident and transmitted flux, respectively), where I_{TR} is measured by a photodiode which can be reproducibly moved in and out of the path of the beam, just downstream from the specimen position. At any energy, the different response of these two detector systems can be compensated for by moving the sample out of the beam and measuring a ‘zero’ absorption ratio for the specimen air gap, a strategy that works as long as both detectors show adequate linearity. In order to gauge measurement uncertainties, the outputs of both detectors were repeatedly measured over a period of time at an energy of 6.9 keV. The movable I_{TR} detector was kept stationary during this time to remove any variability that might come from small repositioning errors and

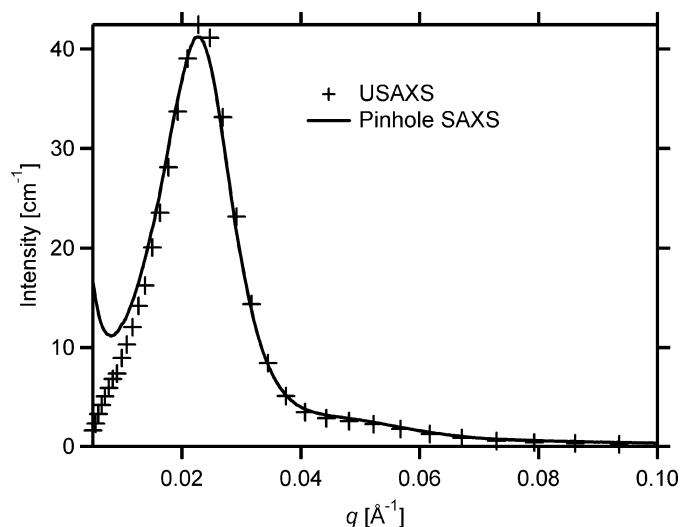


Figure 6 Absolute scattering intensity of the polyethylene standard over a wide energy range.

variations in sensitivity over the photodiode surface. The combined inherent uncertainty of these detectors was found by correlation analysis (Berenson & Levine, 1996) to be 0.04%. Even though these detectors saw different magnitudes of numbers of photons (scattered versus direct beam), the basic counting chains (current amplification followed by voltage-to-frequency conversion and scalar counting) were identical. It is reasonable, therefore, to apportion this variability equally between both detectors.

In practice, early measurements indicated that accurate repositioning of the photodiode detector was crucial, due to gradual radiation damage to the area of the I_{TR} photodiode regularly exposed to the beam. This made the photodiode's sensitivity position-dependent and mechanical positioning errors of a little as 50 μm gave rise to relatively large errors in measured output. Fig. 5 demonstrates how retracting and re-inserting the I_{TR} photodiode dramatically increased this variability. Subsequent improvements in the mechanisms used to insert the I_{TR} detector have reduced mechanical positioning error by more than an order of magnitude. When varying the undulator gap, the beam position varied by only approximately 35 μm across the photon energy range, which helps minimize sensitivity variations of the transmission detector.

2.4. q scaling

Scattering patterns collected on area detectors at fixed camera length provide observed intensities at fixed solid angles. As the photon energy is varied, fixed scattering angles correspond to different vectors in reciprocal space. Data extracted in pixel space were interpolated to fixed q values using a cubic spline method (*XLXTRFUN*; <http://www.xlxfun.com/XIXtrFun/XIXtrFun.htm>) to allow direct comparison or subtraction of intensities at different energies. Because the specimens studied here were isotropic scatterers, interpolation was carried out on radially averaged data. A silver behenate pattern was obtained with every group of ~ 10 specimens at each energy, to verify that beam centring and q scaling were sufficiently energy independent for analysis of tissue specimens.

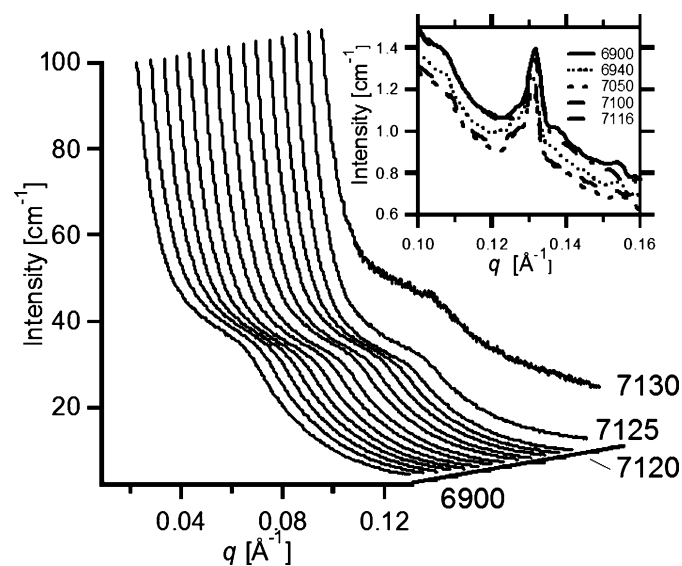


Figure 7
SAXS patterns for a high iron-loaded liver sample ($65.5 \text{ mg Fe g}^{-1}$), and (inset) diffraction peaks from a control liver sample (1.5 mg Fe g^{-1}). Photon energy shown in eV.

3. Absolute intensity standard normalization technique

Scattering standards containing only low atomic number elements (e.g. polyethylene and glassy carbon) lack absorption edges for hard X-ray scattering, and their relatively intense scattering (*i.e.* compared with water) make these standards very suitable for scaling intensities to an absolute scale. As shown in Fig. 6, the absolute scattering intensity of the polyethylene intensity standard used in this experiment was energy independent over a much wider energy range than required for Fe K -edge ASAXS. These measurements were independently calibrated data from a pinhole SAXS camera and a USAXS (ultra small-angle X-ray scattering) instrument operating at a completely different X-ray energy. At each energy of a given ASAXS scan, the intensity calibrant was measured along with all the specimens under comparison, and the well defined peak at 0.0227 \AA^{-1} with an absolute intensity of 41.2 cm^{-1} (Paglia *et al.*, 2004) was used to remove instrument spectroscopic bias.

3.1. Uncertainties

Minimizing and quantifying total measurement uncertainties are important considerations in ASAXS measurements, so that differences in scattering intensities between energies can be evaluated with respect to measurement uncertainties. This is particularly important when using pinhole instruments, as intensity measurements from numerous detectors must be combined.

CCD uncertainties calculated by *SAXS15ID* are two standard errors of the observed variation of individual pixel intensities over each radius used for radial integration (having applied flood-field corrections). Confidence intervals for parameters obtained by linear regression (such as specimen transmissions up to and including 7.100 keV) were determined by statistical analysis of correlations at the 68% level, *i.e.* one standard deviation or one standard error, as appropriate (Berenson & Levine, 1996). Uncertainties in specimen transmissions up to and including 7.100 keV were determined using the standard error of the regression of their observed transmissions with energy, *i.e.* the deviation of mean values of the regression. Above 7.100 keV, the standard deviation of the regression (*i.e.* the prediction interval for individual measurements) was used for specimen transmission uncertainties. For iron-free samples (e.g. polyethylene absolute intensity standard, blank sticky tape or silver behenate), the standard error was used across all measured energies. Uncertainties of I_0 and I_{TR} measurements were determined by linear correlation analysis (Berenson & Levine, 1996). Uncertainties for every intensity measurement were combined to determine total measurement uncertainties.

Data from silver behenate (which is iron free) was used to assess spectroscopic bias in processed data to verify the interpretation of ASAXS data for tissue samples. Repeated measurements of silver behenate, whose data were processed identically to tissue samples, showed that spectroscopic bias was below random uncertainties, or that scattering intensity showed no decrease with increasing photon energy. Systematic decreases in scattering intensity with increasing photon energy were therefore due to iron-scattering contrast change with photon energy and not an artefact of systematic spectroscopic bias.

4. Rat tissue studies

We have been studying a series of iron-loaded rats to gain insight into the iron-loading process. The duration of dietary supplementation or blood transfusion was varied to cause different levels of iron loading.

The details of iron-loading procedures are available elsewhere (Chua-anusorn *et al.*, 1999).

Specimens were prepared from freeze-dried tissue that had been ground into a powder and then pelletized to controlled thickness and density, and mounted between two layers of adhesive tape. SAXS data were collected at up to ~16 incident photon energies between 6.900 and 7.140 keV using 15-ID-D at the APS configured as above. Data for silver behenate and a calibrated polyethylene intensity standard were also acquired with every group of specimens at every energy. Two camera lengths (547 and 1875 mm) were used over the nominal q ranges of 0.005–0.18 and 0.022–0.6 Å⁻¹, respectively. Collection times varied between 2 and 10 s per pattern. Results presented here demonstrate the viability of this technique in the current application and illustrate the capability of the instrument. The bulk of our data and their contribution to iron-overload research will be reported elsewhere (Bovell *et al.*, 2006).

4.1. Results

SAXS patterns for several liver specimens with increasing iron loadings are shown in Fig. 2. These patterns were taken at 6.900 keV, which maximizes scattering contrast between iron-rich and organic structures. The control specimen displayed several Bragg peaks, the most visible of which was at ~0.13 Å⁻¹, whose intensities varied on iron loading. The intensity of a broad shoulder at approximately 0.06 Å⁻¹ increased with iron loading. These observations, which are also readily obtainable on laboratory instrumentation, show various effects of iron loading on scattering patterns but do not reliably indicate the nature of the structures from which they arise. Differences in scattering patterns due to iron-rich nanoparticles were distinguished from other physiological effects on tissues by the energy dependence of scattering intensities close to the Fe *K*-edge.

The energy dependence of scattering patterns for a high iron-loaded liver sample is shown in Fig. 7. The systematic reduction in the scattering intensity of the feature at 0.06 Å⁻¹ is consistent with the decrease in f' approaching the absorption edge, and is due to iron-rich structures and not to instrument spectroscopic bias. This feature was observed in all iron-loaded specimens, and its magnitude correlated with iron-loading. Use of scattering data above the absorption edge (e.g. 7.12 keV), was impractical, due to high specimen absorption and background fluorescent intensity. Random errors in trans-

missions and the number of pixels recording data near the beamstop restricted analysis below 0.02 Å⁻¹.

Fe-*K* edge ASAXS was readily able to determine features arising from non-iron structures (*i.e.* whose net intensity was energy independent), their q scaling, and their magnitude as a function of iron-loading. An example of non-iron Bragg peaks is shown in the inset in Fig. 7. These peaks, most readily observable in control specimens, were rapidly affected by iron loading, demonstrating that ASAXS was capable of discriminating secondary effects on tissue structures due to excessive iron-loading. The q position of the main Bragg peak at 0.13 Å⁻¹ suggests this may be due to some type of lipid, but reliable identification requires external information. The constant net intensity of Bragg peaks in control samples illustrates effective mitigation of instrument spectroscopic bias.

The data can be modelled successfully with the unified model (Beaucage, 1995) using *IRENA* (Version 2.10; <http://www.uni.aps.anl.gov/~ilavsky/irena.html>). Data were modelled by fitting a power law and correlated Guinier knee for level 1 ($q > 0.015$ Å⁻¹), and a power law with an R_g (radius of gyration) cutoff of 25 Å for level 2 ($q < 0.015$ Å⁻¹); explanations for level 1 and level 2 can be found in Beaucage (1995). An example shown in Fig. 8, which indicates the feature at ~0.06 Å⁻¹, can be modelled as a Guinier knee, with R_g ranging between 23–28 Å over the suite of samples analysed, corresponding to spherical iron-rich particles of 5.8–7.1 nm diameter, comparable with TEM analysis (5.5±0.5 nm). The G parameter in the unified model as implemented in *IRENA* is directly proportional to the size of the Guinier knee. The size of the Guinier knee correlated both with iron loading and with photon-energy dependence (Fig. 9), which shows excellent experimental agreement between the energy dependence of G and the expected decrease in f' . The observed minimum in iron scattering power was at the inflection point of the absorption edge. Thus, the Guinier knee is due to the presence of iron-rich particles, and is not caused by secondary biological effects on organic tissue structures. The rather large number of energies used to establish the validity of the measurement would most probably not be required for routine analysis.

ASAXS facilitated bulk analysis of all particles in tissues, overcoming the difficulty of measuring the sizes of particles packed in clusters by TEM. It also provided a simple parameterized measure of

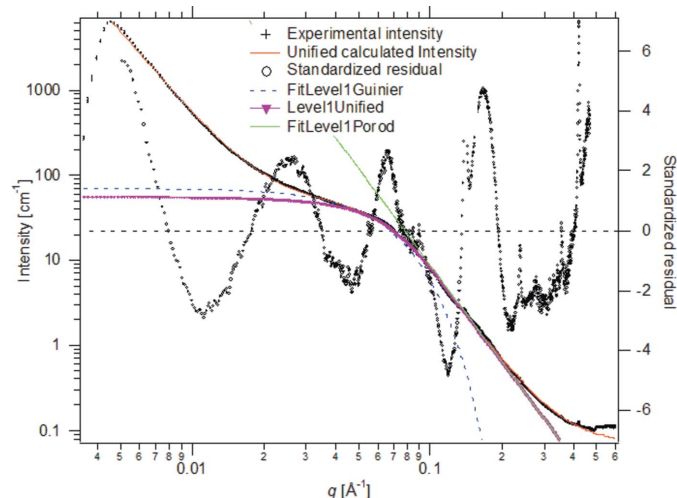


Figure 8 Unified model of combined q range for a high iron-loaded liver sample.

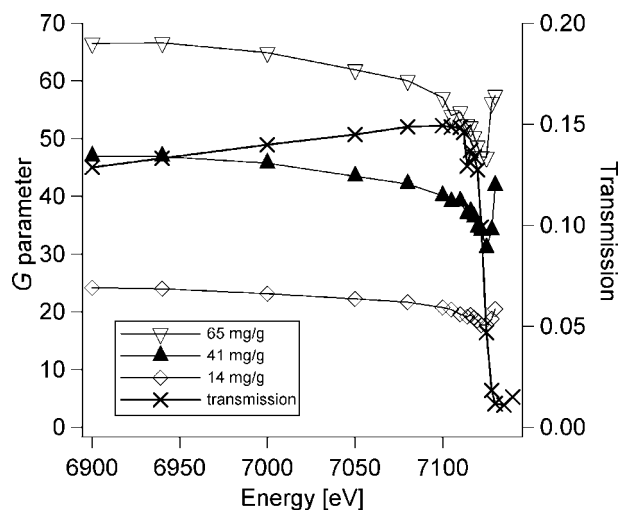


Figure 9 Magnitude of the Guinier knee (unified model G parameter) from iron-rich nanoparticles as a function of photon energy and iron loading. Transmission is shown for the most iron-rich specimen (65 mg Fe g⁻¹).

local packing structure. Modelling indicates particles were spatially correlated (the characteristic spacing was typically ~ 90 Å), due to relatively close but poorly ordered (packing factor ~ 1) packing of primary particles within clusters, particularly in highly loaded specimens. Detailed analysis of scattering patterns, to quantify structural information on the iron particles (such as average sizes, packing correlations, trends of structural parameters with iron loading *etc.*) are to be reported elsewhere (Bovell *et al.*, 2007).

5. Conclusions

With careful experimental technique, 15-ID-D is a reliable instrument for ASAXS analysis, including Fe *K*-edge ASAXS. Techniques for analysis of iron particles in tissue samples were developed that allowed for the management of spectroscopic bias and provided acceptable measurement uncertainties even at relatively low levels of iron loading. Numerous instrument parameters were analysed to determine optimal data-collection and processing strategies, allowing the technique to be available to users. ASAXS data allowed reliable differentiation between scattering from iron-rich particles and non-iron tissue structures, as well as an assessment of the primary particle size and local packing arrangement of iron particles as a function of disease state and iron loading. Primary iron particle sizes were in good agreement with those obtained by TEM analysis. The 15-ID-D instrument and the data-collection and processing strategies reported will be useful for reliable ASAXS data on complex mixed-phase samples in the biological and physical sciences.

Dr Jan Ilavsky (UniCAT, APS) kindly provided USAXS measurements in support of this work, and is the author of *IRENA* software used extensively in data analysis. NK acknowledges the support of the Australian Synchrotron Research Programme for an ASRP Postdoctoral Fellowship and travel support. This work was partly supported by the Australian Research Council (grant No. DP0451535). The Bruker AXS Nanostar instrument at Curtin University was funded by the Australian Research Council RIEF (grant No. R00107962). Use of the ChemMatCARS sector 15 at the APS was supported by the Australian Synchrotron Research Programme, which is funded by the Commonwealth of Australia

under the Major National Research Facilities Programme. ChemMatCARS Sector 15 is principally supported by the National Science Foundation/Department of Energy under grant No. CHE0087817. The APS is supported by the US Department of Energy, Basic Energy Sciences, Office of Science, under Contract No. W-31-109-Eng-38. Dr Martin Saunders of the University of Western Australia provided valuable assistance with TEM analysis. Amanda Kirby assisted with ASAXS data collection. Dr Wanida Chua-anusorn of the University of Western Australia kindly made the rat samples available for this study.

References

- Als-Nielsen, J. & McMorrow, D. (2001). *Elements of Modern X-ray Physics*, p. 235. Chichester: Wiley.
- Beaucage, G. (1995). *J. Appl. Cryst.* **28**, 717–728.
- Berenson, M. L. & Levine, D. M. (1996). *Basic Business Statistics, Concepts and Applications*, 6th Edition, pp. 726–750. New Jersey: Prentice Hall.
- Berg Rasmussen, F., Molenbroek, A. M., Clausen, B. S. & Feidenhans, R. (2000). *J. Catal.* **190**, 205–208.
- Berg Rasmussen, F., Sehested, J., Teunissen, H. T., Molenbroek, A. M. & Clausen, B. S. (2004). *Appl. Catal. A*, **267**, 165–173.
- Bovell, E., Kirby, N. M., Cookson, D., Buckley, C. E. & St. Pierre, T. (2007). In preparation.
- Bruckner, R., Lembke, U. & Kranold, R. (1995). *Nucl. Instrum. Methods Phys. Res. B*, **97**, 190–193.
- Chua-anusorn, W., Macey, D. J., Webb, J., de la Motte Hall, P. & St Pierre, T. G. (1999). *Biometals*, **12**, 103–113.
- Cookson, D., Kirby, N., Knott, R., Lee, M. & Schultz, D. (2006). *J. Synchrotron Rad.* **13**, 440–444.
- Grootveld, M., Bell, J. D., Halliwell, B., Arouma, O. I., Bomford, A. & Sadler, P. J. (1989). *J. Biol. Chem.* **264**, 4417–4422.
- Halliday, J. W. & Powell, L. W. (1992). *Haemochromatosis and Other Diseases Associated With Iron Overload. Iron and Human Disease*, pp. 132–60. Boca Raton: CRC Press.
- Jemian, P. R. (1990). PhD Dissertation, Northwestern University, Illinois, USA.
- Krosigk, G. V., Cunis, S., Gehrke, R. & Kranold, R. (2001). *Nucl. Instrum. Methods Phys. Res. A*, **467–468**, 1088–1091.
- Paglia, G., Buckley, C. E., Udovic, T. J., Rohl, A. L., Jones, F., Maitland, C. F. & Connolly, J. (2004). *Chem. Mater.* **16**, 1914–1923.
- Servant, C., Lyon, O. & Simon, J. P. (1989). *Acta Metall.* **37**, 2403–2411.
- Sheppard, D. A., Maitland, C. F. & Buckley, C. E. (2005). *J. Alloys Compd.* **404–406**, 405–408.
- Stuhrmann, H. B. (1981). *Q. Rev. Biophys.* **14**, 433–460.